Journal of Applied Physics

RESEARCH ARTICLE | OCTOBER 08 2024

Gradient descent optimization of acoustic holograms for transcranial focused ultrasound

Ahmed Sallam ; Ceren Cengiz ; Mihir Pewekar ; Eric Hoffmann; Wynn Legon ; Eli Vlaisavljevich ; Shima Shahab

J. Appl. Phys. 136, 144901 (2024)
https://doi.org/10.1063/5.0220486

Journal of Applied Physics | ARTICLE | pubs.aip.org/aip/jap

Gradient descent optimization of acoustic holograms for transcranial focused ultrasound

Cite as: J. Appl. Phys. **136**, 144901 (2024); doi: 10.1063/5.0220486
Submitted: 25 May 2024 · Accepted: 19 September 2024 ·
Published Online: 8 October 2024

Ahmed Sallam,[1] Ceren Cengiz,[1] Mihir Pewekar,[1] Eric Hoffmann,[1] Wynn Legon,[2] Eli Vlaisavljevich,[3] and Shima Shahab[1,a)]

AFFILIATIONS

[1]Department of Mechanical Engineering, Virginia Tech, Blacksburg, Virginia 24061, USA
[2]Fralin Biomedical Research Institute, Virginia Tech, Roanoke, Virginia 24016, USA
[3]Department of Biomedical Engineering and Mechanics, Virginia Tech, Blacksburg, Virginia 24061, USA

[a)]**Author to whom correspondence should be addressed:** sshahab@vt.edu

ABSTRACT

Acoustic holographic lenses, also known as acoustic holograms, can change the phase of a transmitted wavefront in order to shape and construct complex ultrasound pressure fields, often for focusing the acoustic energy on a target region. These lenses have been proposed for transcranial focused ultrasound (tFUS) to create diffraction-limited focal zones that target specific brain regions while compensating for skull aberration. Holograms are currently designed using time-reversal approaches in full-wave time-domain numerical simulations. Such simulations need time-consuming computations, which severely limits the adoption of iterative optimization strategies. In the time-reversal method, the number and distribution of virtual sources can significantly influence the final sound field. Because of the computational constraints, predicting these effects and determining the optimal arrangement is challenging. This study introduces an efficient method for designing acoustic holograms using a volumetric holographic technique to generate focused fields inside the skull. The proposed method combines a modified mixed-domain method for ultrasonic propagation with a gradient descent iterative optimization algorithm. The findings are further validated in underwater experiments with a realistic 3D-printed skull phantom. This approach enables substantially faster holographic computation than previously reported techniques. The iterative process uses explicitly defined loss functions to bias the ultrasound field's optimization parameters to specific desired characteristics, such as axial resolution, transversal resolution, coverage, and focal region uniformity, while eliminating the uncertainty associated with virtual sources in time-reversal techniques. The proposed techniques enable more rapid hologram computation and more flexibility in tailoring ultrasound fields for specific therapeutic requirements.

I. INTRODUCTION

Transcranial focused ultrasound (tFUS) is a transformative technology that employs concentrated ultrasound energy to treat various neurological conditions.[1,2] Non-ionizing acoustic beams can penetrate through the skull and precisely target specific structures deep within the brain. The energy of the ultrasound beam elicits thermal and mechanical effects in brain tissue. Those effects are utilized for a variety of therapeutic treatments and procedures. At lower intensities, tFUS can accurately transmit energy to specific regions in the brain and induce local modulation of neural activity.[3–6] Furthermore, tFUS has been demonstrated to locally disrupt the blood–brain barrier (BBB),[7–10] allowing for improved delivery of therapeutic drugs. High-intensity ultrasound is also leveraged in tFUS to treat various diseases and disorders,[1] for which ultrasound energy can be used to thermally ablate diseased tissue,[11] and high pressures can be used for histotripsy,[12–14] in which targeted tissues are mechanically fractionated.

Focusing the ultrasound beam in tFUS presents challenges because of the highly rigid nature of the skull, characterized by its high acoustic impedance, irregular geometry, and nonuniform thickness, which strongly scatter and attenuate the propagating ultrasound beam. This phenomenon is known as skull-induced aberrations,[15,16] and it causes severe defocusing and phase distortion of the beam, resulting in inefficient and out-of-target focusing. To address this issue, 3D-printed acoustic holographic lenses,

known as acoustic holograms, have been recently proposed for compensation of skull aberrations in tFUS applications.[17–23] Acoustic holograms act like phase plates, modulating the phase of the wavefront with unique thickness maps. The thickness map enables the reconstruction of complicated acoustic fields with a desired spatial distribution of pressure or phase using a single-element acoustic transducer. These lenses have been shown to modulate reflected and transmitted wavefronts,[24–27] forming multi-focal spots or arbitrary complex patterns for applications such as contactless ultrasound energy transfer,[28] particle manipulation,[27,29] controlling cavitation zones,[30] and hyperthermia.[31,32] These intricate modulation and manipulation capabilities make them ideal for tFUS applications. The acoustic lens compensates for skull aberrations and creates highly localized pressure fields that direct the ultrasound beam to specific brain areas within the skull. Acoustic holograms offer high-resolution, diffraction-limited focusing capabilities. Although they lack the real-time control and focus steering found in phased array transducers, their significantly lower costs and simpler fabrication processes are highly desirable.[27] They have been tested successfully in bench-top setups using 3D-printed phantoms and *ex vivo* human skulls,[22,23] as well as *in vivo* mouse models[20,21] for neuromodulation and BBB opening procedures.

Time-reversal numerical simulations and direct error minimization techniques are currently employed to generate an appropriate thickness map that accounts for skull aberrations and directs the ultrasonic field to the target structure in the brain. In the numerical domain, monopole virtual sources are introduced at the target regions of the skull. The ultrasound is then transmitted from the simulated sources to the hologram plane outside of the skull, where the acoustic signal is recorded. The extracted signal is subsequently processed to determine the phase and amplitude distributions in the hologram plane. The phase and amplitude information are then used to construct the lens thickness map. Ultrasound propagation in strongly heterogeneous media is often carried out using full-wave numerical simulations, namely, the pseudospectral time-domain method implemented in the open-source software k-Wave.[33] However, full-wave numerical simulations are computationally expensive, lasting up to 20 h when using CPU parallel processing.[22] The long computation time also prevents the use of iterative optimization techniques, which could help improve focusing quality and allow the implementation of explicitly specified loss functions to bias the ultrasound field's optimization parameters to specific desired characteristics, such as axial resolution, transversal resolution, coverage, and focal region uniformity. Furthermore, iterative algorithms take into account the transducer's experimental amplitude output, improving the accuracy of the thickness map and eliminating the need for error diffusion schemes.

Acoustic holography is a technique that allows for the reconstruction of 3D acoustic fields by projecting measured or simulated 2D data from a measurement plane to the remainder of the volume.[34] Because of its computing efficiency, holography is used in iterative optimization techniques such as the Gerchberg–Saxton (GS) and iterative angular spectrum algorithms to compute and design the thickness map of holographic lenses.[27,29] In those techniques, the wavefront is iteratively propagated forward and backward between the hologram and target planes until a satisfying boundary condition is obtained. However, such techniques are intended for freely propagating media and optimizing planar pressure patterns.

This paper introduces an analogous iterative optimization approach that takes into account strongly heterogeneous media and aberrating layers, including the effects of reflection, transmission, scattering, and attenuation. Furthermore, the proposed method optimizes for volumetric targets, such as directing sound to specific volumetric components in the brain. The modified mixed domain method (MMDM)[35–37] is used to simulate the forward and backward propagation inside the strongly heterogeneous media. In addition, a non-convex gradient descent optimization algorithm is used to find the optimal phase for targeting a specific volume. The proposed technique is substantially more efficient, allowing for the creation of a hologram in less than 50 min while also allowing for the explicit defining of loss functions. The proposed algorithm is evaluated numerically by considering four test cases that target different brain structures: the anterior insula, hippocampus, caudate nucleus, and amygdala. Each target resides at a different depth in the brain and has a distinct complex volume and geometric structure in 3D space. The holographic lenses obtained for each target are then 3D printed and tested in underwater trials and on a 3D-printed skull phantom.

II. METHODS

A. Acoustic propagation

The MMDM[35–38] is used to carry out computationally efficient forward and backward propagations through the strongly heterogeneous domain, which includes the skull and water. This methodology is implemented in the open-source MATLAB toolbox mSOUND,[37] which has been employed for the present study. For linear acoustic propagation, the MMDM solves the Helmholtz equation with the absorption term. For arbitrarily heterogeneous media, the MDMM accounts for the reflection and transmission of the wavefront locally at each propagation step on a Cartesian spatial mesh. Sources are modeled by assigning a complex pressure distribution on the source plane, in a manner analogous to the angular spectrum method. All simulations conducted in this study utilized the mSOUND MATLAB functions *Forward3D_fund* and *Backward3D_fund* to perform the forward and backward propagations, respectively. Non-propagating evanescent waves are filtered out through spatial filtering intrinsic to the mSOUND toolbox.

B. Hologram computation

Computer-generated holography (CGH) can be implemented to construct desired 3D pressure patterns by altering the wavefront of a coherent acoustic beam.[29] CGH determines the spatial phase and amplitude distribution of an incident wavefront, which, upon diffraction, forms the target volume. Computing the 2D phase mask that yields certain intensity patterns is generally a non-trivial and ill-posed task.[39] Most three-dimensional intensity patterns are not physically viable. The wave field must diffract through space in a way that is consistent with Helmholtz's equations and maintains intensity conservation at each depth plane. Furthermore, resolution is limited due to the finite numerical aperture (NA). The phase-only hologram constraint also compounds these limitations

further. As a result, any required 3D pressure pattern cannot be precisely reproduced. The optimal thickness map for the 3D-printed hologram is determined by optimizing the output acoustic field under experimental limitations such as incident beam profile, source NA, and wave shaping modality. Following prior efforts in acoustics and optics, we use a gradient descent optimization approach in the present investigation.[29,39]

The defined loss function greatly influences the outcomes of 3D CGH, where there is no exact solution but many approximate solutions. The algorithm searches for optimal holograms using custom cost functions that can be formulated and modified based on the desired optimization goals. The optimization aims to obtain a phase distribution ϕ at the hologram plane that minimizes a specified error function $L[P3D(\phi), T]$ between the generated acoustic field $P3D(\phi)$ in the volumetric domain and the volumetric target pattern T, with the constraint that the pressure amplitude at the transducer plane must always equal to the experimental pressure $|p_0| = A_0$. The numerical solution of this optimization problem necessitates calculating the gradient of the loss function with respect to the decision variables. First, a square loss function is assumed,

$$L(P3D, T) = \frac{1}{2}\sum_{i=1}^{n_X}\sum_{j=1}^{n_Y}\sum_{k=1}^{n_Z}\left(P3D_{ijk} - T_{ijk}\right)^2, \tag{1}$$

implementing Wirtinger subdifferential calculus and following the derivation in Ref. 29, the gradient of the loss function L is calculated as

$$\nabla L = 2A^*\left(P3D - T \circ \frac{P3D}{|P3D|}\right), \tag{2}$$

where A^* represents the backward propagation from each plane in the volume back to the transducer plane such that $A^*P3D = p_0$.

This algorithm is analogous to the GS algorithm and follows similar steps. However, with the aid of the MMDM, this algorithm correctly takes into account the heterogeneity of the media. In words, the algorithm's steps are as follows: (1) propagate the pressure from the transducer plane to the rest of the volume, (2) calculate the gradient of the loss function and backpropagate each plane in the volume back to the hologram plane and obtain the new phase distribution at the transducer plane, (3) impose the new phase distribution and the initial transducer amplitude at the transducer plane, and (4) repeat steps 1–3 until the desired convergence criterion is met.

The algorithm output provides a phase map at the hologram plane which can then be transformed to a thickness map for fabrication. The resulting thickness map is calculated as:[27] The holographic plate starts with an initial thickness T_0. Removing material at pixel position (X, Y) causes a relative phase change of

$$\Delta\phi(X, Y) = (k_m - k_h)\Delta Th(X, X),$$

where $Th(X, Y) = Th_0 - \Delta Th(X, Y)$ is the thickness of the pixel positioned at coordinates (X, Y) in the hologram plane and k_h, k_m are the wave numbers in the hologram and its surrounding medium, respectively.

III. NUMERICAL RESULTS

A flat single-element transducer combined with an acoustic hologram can correct for skull aberrations and create a focal point tailored to a certain target location and volume. The geometry of the skull is derived from a computed tomography (CT) scan of an *in vivo* subject and processed to a resolution of the numerical grid. The skull geometry is sliced along a plane parallel to the sagittal plane [see Fig. 1(b)] to match the 3D-printed skull in the experimental setting. The skull section is integrated into the numerical

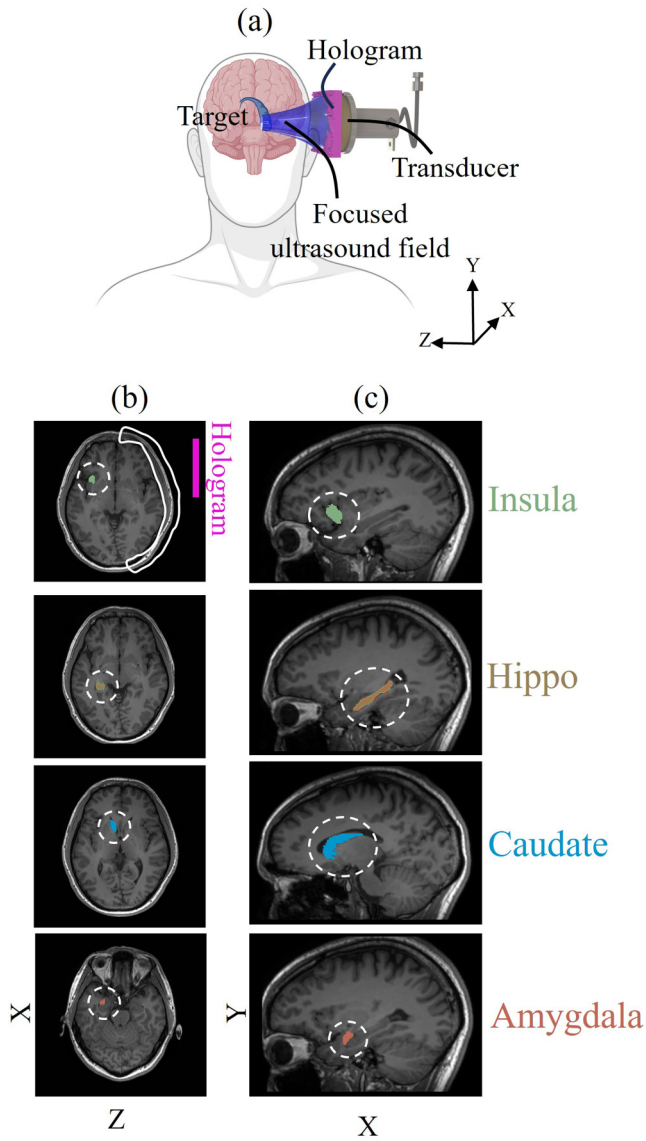

FIG. 1. (a) The schematic representation of the concept. (b) Axial and (c) transverse sections of the MRI scans. The target volumes' geometries are emphasized in distinctive colors.

simulations with a resolution of 0.5 mm, which corresponds to $\lambda/6.67$ for the transducer drive frequency in water. The numerical grid's resolution is uniform in all directions ($dX = dY = dZ$). Two orders of reflection were considered in all of the simulations. The geometry and placement of the therapeutic targets chosen for this investigation have been retrieved from the magnetic resonance imaging (MRI) scans and fitted and mapped into their proper locations in the cranial cavity. The flat circular transducer and hologram are situated at the temporal bone window, at a distance of 15 mm between the hologram's surface and the skull's surface. The respective locations of the transducer and the hologram are shown in a schematic representation in Fig. 1(a). The transducer's output is experimentally evaluated in a water tank, with hydrophone measurements taken at an excitation frequency of 444 kHz.

The numerical algorithm is constrained by the transducer's measured experimental amplitude, and the thickness map is designed using the initial experimental phase, as detailed in Algorithm 1. In all simulations, the average amplitude at the transducer's surface is normalized to 1 Pa. Water is assumed everywhere else in the numerical domain since it is a good approximation of soft tissue and matches the water-submerged experiments. The acoustical properties of the 3D printing material (refer to Sec. IV A) are used for the skull to match the experimental and simulation parameters. The domain dimensions consist of 384 grid points in the X direction, 212 grid points in the Y direction, and 199 grid points in the Z direction.

For the proposed gradient optimization combined with the MMDM method, the Armijo line-search parameters are set to $\beta = 0.9$ and $\sigma = 0.002$ with an initial step size of $\tau = 1$. The target volume T is a binary volumetric matrix with nonzero values at the targeted brain structure. The numerical simulations of acoustic propagation are performed using the MMDM and implemented in the open-source toolbox mSOUND on MATLAB R2019b.[37] A computational node equipped with AMD EPYC 7702 2.5 GHz (total of 18 cores) and 36 GB of RAM is used for all simulations. In the proposed algorithm, the backward propagation stage consumes the most processing time. The pressure at each plane in the entire volume must be propagated back to the transducer plane. Because each propagation is independent, a parallel backpropagation technique was created using MATLAB's *parfor* function, which considerably accelerated the procedure. In the current study, each iteration lasted an average of 380 s, and each simulation produced satisfactory results, based on the quantitative metrics outlined in Table I, after seven iterations on average. The average overall simulation time was 44 min.

To assess the proposed algorithm's performance, we investigate four separate test cases involving various targets inside the brain. We created four distinct holograms that focus the ultrasound field on the anterior insula, hippocampus, caudate nucleus, and amygdala. Each of these targets has distinct properties in terms of shape, volume, orientation, and spatial placement within the brain structure. This diversity allows for a more comprehensive and general assessment of the holograms' performance capabilities. We shall look at the axial and transversal distribution of the ultrasonic field within the brain. In addition, we look into the sonication volume and peak focal pressure gain inside and outside the target regions. Sonication volumes are calculated as the region with a pressure gain of at least −3 dB with respect to the peak pressure in the brain for each test instance. Normalized peak pressure is calculated as the pressure gain relative to the average pressure at the transducer surface. Summary of the numerical results are in Table I and the results of the numerical simulations for all the test cases with and without the hologram are summarized in Fig. 2. It is important to note that cases without the hologram are included to demonstrate the capability of acoustic holograms to tailor the pressure field as desired, but are excluded from the performance analysis since they do not provide a fair comparison [see Figs. 2(a.1) and 2(a.2) for the normalized pressure fields featuring only a flat transducer].

A. Anterior insula

The anterior insula is a brain area that processes taste, emotions, and interoceptive awareness, including hunger and pain. It also plays roles in autonomic functioning and sensory processing, including auditory and vestibular functions, and is essential for empathy and social cognition.[40,41] In the present simulation, the insula's volume is 0.875 cm^3, and it is positioned at a depth of 8.32 cm from the hologram's surface along the axial direction, making it the deepest target among all the test cases. The dimensions of the insula extend to lengths of 0.9, 1.9, and 1 cm along the X, Y, and Z axes, respectively. The segmented MR image with the highlighted geometry of the anterior insula is illustrated in Figs. 1(b) and 1(c). The normalized cross-section of the maximum pressure field in the YZ and XY planes are shown in the first row of Figs. 2(b.1) and 2(b.2), respectively. Each cross section intersects the centroid of the target volume. The cartesian axes are aligned with the axes of the source. As illustrated in the axial and transversal cross sections, the pressure is concentrated on the insula volume, which is marked by the white dashed line. Good coverage is obtained, with the main focal encompassing the majority of the

TABLE I. Summary of the numerical results.

	Volume (cm^3)	Total sonicated volume (cm^3)	Sonication inside target (cm^3)	Target sonication (%)	Gain inside target	Gain outside target
Insula	0.875	2.7	0.45	51.4	4.55	4.67
Hippocampus	3.85	9.9	1.61	41.8	2.97	3.15
Caudate	4.73	8.81	1.2	25.4	3.32	3.38
Amygdala	0.491	2.22	0.321	65.3	5.49	5.49

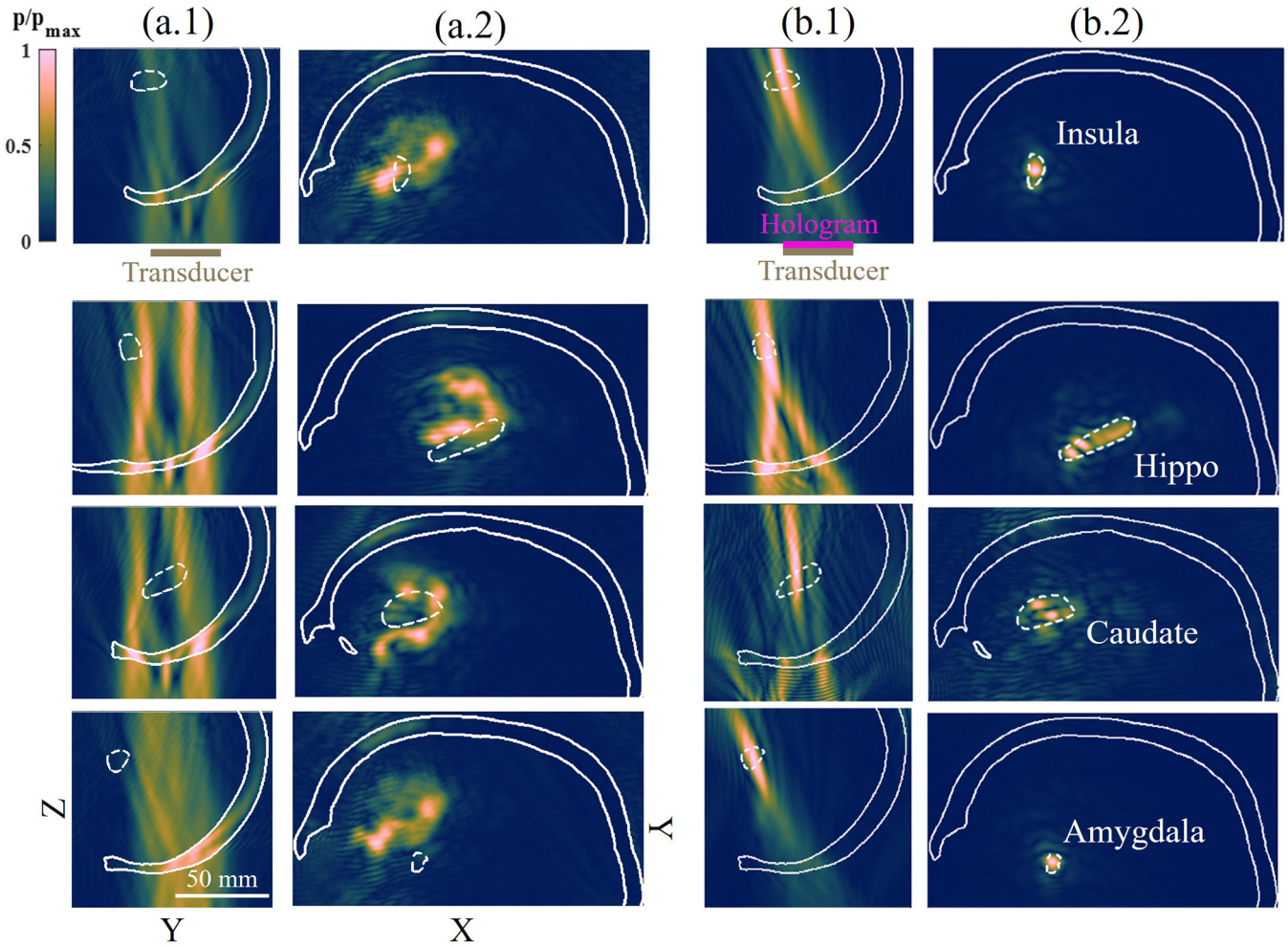

FIG. 2. Summary of the numerical findings for targeting the desired volumes within the skull phantom with and without the hologram. Columns (a.1) and (a.2) show the axial and transverse sections of the normalized pressure field without the hologram incorporated, respectively. Columns (b.1) and (b.2) depict the localized pressure field when the hologram is added to the domain. The dashed line represents the desired volume, whereas the solid white line represents the skull phantom.

volume. However, while the energy is focused on the Insula, significant acoustic pressure occurs both before and after the focal zone. The maximum normalized pressures inside and outside the target volume are close, at a value of 4.55 and 4.67, respectively. A total of 0.45 cm^3 of the insula was sonicated, representing 51.4% of the total volume. While 2.25 cm^3 was sonicated outside the target. It is also important to note the low-pressure amplitudes seen in the skull (which is outlined by solid white lines). This is crucial since it reduces the possibility of skull heating effects, which improves the therapeutic technique's safety profile.

B. Hippocampus

The hippocampus, located in the temporal lobe of the brain, is responsible for memory formation and storage, spatial navigation, and stress and mood regulation. It also affects the learning process. Dysfunction in this area can lead to memory issues, spatial disorientation, and emotional problems.[42] The volume of the segmented hippocampus is 3.85 cm^3, and it is located at a depth of 7.55 cm from the hologram's surface along the axial direction. The dimensions of the hippocampus extend to lengths of 4.45, 2.55, and 1.55 cm along the X, Y, and Z axes, respectively. MRI scans, presented in Figs. 1(b) and 1(c), show that the hippocampus extends more prominently in the transversal plane along the X axis. At 4.45 cm, the hippocampus is the largest in terms of length in the X direction among all the target volumes investigated. The normalized cross section of the maximum pressure field in the YZ and XY planes are shown in the second row of Figs. 2(b.1) and 2(b.2), respectively. The axial and transverse cross sections clearly show the pressure focus within the hippocampus volume. The transverse

cross section shows that pressure is effectively contained inside the intended area. However, axially, substantial pressure exists outside the target zone. The maximum normalized pressure inside and outside the target volume are close, at a value of 2.97 and 3.15, respectively. Using the hologram 1.61 cm^3 or 41.8% of the hippocampus is sonicated. However, a significant portion of the sonicated volume, amounting to 8.1 cm^3, occurs outside the targeted region, with 83.4% of the total sonicated volume falling outside the intended area. Furthermore, high-pressure amplitudes in the skull increase the risk of causing unwanted skull heating effects when performing therapeutic operations.

C. Caudate nucleus

The caudate nucleus in the brain's basal ganglia is crucial for motor control, procedural learning, reward processing, decision-making, and emotional processing. Its dysfunction is associated with various neurological and psychiatric disorders, including Parkinson's and Huntington's diseases.[43] The volume of the segmented caudate nucleus is 4.73 cm^3, and it is positioned at a depth of 6.2 cm from the hologram's surface along the axial direction, making it the largest target and the closest to the hologram surface among all the targets considered in the present investigation. The dimensions of the caudate extend to lengths of 4.1, 2.3, and 1.75 cm along the X, Y, and Z axes, respectively. MRI scans, as presented in Figs. 1(b) and 1(c), show that the caudate also extends more prominently in the transversal plane along the X axis. The normalized cross section of the maximum pressure field in the YZ and XY planes are shown in the third row of Figs. 2(b.1) and 2(b.2), respectively. The axial and transverse cross sections show the pressure concentration inside the caudate's volume, however, there is less effective coverage of the target area than in earlier tests. This is emphasized by the relatively smaller sonicated volume of the caudate, amounting to 1.2 cm^3 or 25.4% of its total volume. This level of sonication is notably the lowest among all the considered test cases. The sonicated volume outside of the target volume is 8.81 cm^3 which is 86.3% of the total sonicated volume. The maximum normalized pressure inside and outside the target volume are close, at a value of 3.32 and 3.38, respectively.

D. Amygdala

The amygdala, a tiny region in the brain, is critical in emotional processing, notably fear and aggression. It is essential for developing emotional memories and influencing decision-making. The amygdala is also involved in stress and anxiety reactions, as well as social interactions through the interpretation of social cues. Amygdala dysfunction can cause emotional disorders, memory problems, and difficulties with social behavior.[44] The volume of the segmented amygdala is 0.491 cm^3, and it is positioned at a depth of 7.49 cm from the hologram's surface along the axial direction. The dimensions of the amygdala extend to lengths of 0.8, 1.2, and 1.15 cm along the X, Y, and Z axes, respectively. The amygdala is the smallest and most contained target volume among all the test cases, as highlighted by the MRI scans in Figs. 1(b) and 1(c). The normalized cross section of the maximum pressure field in the YZ and XY planes are shown in the fourth row of Figs. 2(b.1) and 2(b.2), respectively. The axial and transversal cross sections demonstrate adequate coverage and containment of the focus zone in the target region. This is highlighted by the high sonication rate within the amygdala with a total sonication volume of 0.32 cm^3 or 65.3%, which is the highest sonication percentage among all the test cases. The sonicated volume outside of the target volume is 1.93 cm^3, which represents 85.8% of the total sonicated volume. The maximum normalized pressure inside and outside the target volume is the same, at 5.49, which is the largest gain achieved among all test cases. Low-pressure amplitudes in the skull were also observed when targeting the amygdala.

E. Effect of skull aberration

To verify that the proposed algorithm effectively compensates for skull aberrations, a hologram for each target is optimized assuming a homogeneous media with no skull. The skull is then inserted into the domain and the acoustic field generated by each hologram is simulated. Figures 3(a.1) and 3(a.2), respectively, show the acoustic field of the initial homogeneous simulation and when the skull is inserted in the numerical domain. The effect of the skull aberrations can be observed as a shift in the focus and degraded coverage of the target region. The calculated targets sonication after the insertions of skull are compared to the MMDM results in Table II. Improved sonication in all targets is achieved using the proposed algorithm which highlights effective compensation for aberrating layers. Illustrations of the pressure field for all targets can be found in Fig. S2 in the supplementary material.

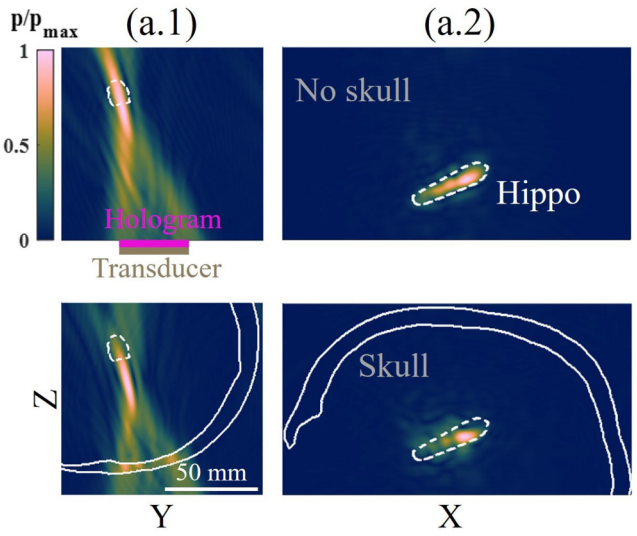

FIG. 3. Numerical results for demonstrating the effect of skull aberration. The pressure field distribution is displayed for the case optimized without the skull, followed by testing the designed hologram with no skull included in the numerical domain. Targeting is shown in (a.1) axial and (a.2) transversal views for comparison.

TABLE II. Effect of skull aberrations.

	Volume (cm^3)	Target sonication (%)	
		Homogeneous	MMDM
Insula	0.875	39.51	51.4
Hippocampus	3.85	22.69	41.8
Caudate	4.73	19.36	25.4
Amygdala	0.491	40.70	65.3

F. Time-reversal simulations

To compare the computational cost and focusing performance of the proposed algorithm against previously demonstrated time-reversal techniques,[22,45] we performed time-reversal numerical simulations for generating four acoustic holograms using three-dimensional k-space pseudospectral linear simulations implemented in the open-source MATLAB toolbox k-Wave.[51] A computational node equipped with AMD EPYC 7702 2.5 GHz (total of 64 cores) and 256 GB of RAM is utilized for all k-wave simulations in MATLAB R2019b. It should be noted that the computational resources for these simulations were significantly larger due to the requirements of the full-wave time-domain numerical techniques.[37,38] The total computational time required for the reversal and forward propagation steps was 4.5 h, which is approximately six times slower than the MMDM proposed algorithm. The calculated target sonication using the time-reversal generated holograms is summarized in Table III. The holograms generated using the proposed algorithm achieved significantly better sonification levels in the insula, caudate, and amygdala compared to the time-reversal. The sonication levels of the hippocampus were similar for both methods. We also note the low sonication level of the caudate at 3% using time-reversal. After inspecting the pressure field, this has been attributed to the presence of high amplitude pressures in the skull. Illustrations of the pressure field for all targets can be found in Fig. S1 in the supplementary material.

G. Multi-focal targeting

In addition to compensating for skull aberrations, acoustic holograms can generate intricate multi-focal pressure patterns which opens up the opportunity for simultaneous targeting of multiple structures in the brain. To this end we consider two case studies, in the first, we generate a hologram to simultaneously target the four previously considered brain structure as shown in Fig. 4. Furthermore, in the second case a hologram is generated to simultaneously target the Hippocampus and the amygdala as shown in Fig. 5. In Fig. 4 as expected, the focusing of the acoustic energy is degraded when many targets are considered. Though it can be observed that the acoustic field is shaped around the desired targets, the acoustic pressure does not cross the −3 dB sonication threshold in the overwhelming majority of the target volumes which leads to a low total volume sonication level of 7.82%.

TABLE III. Time-reversal simulations.

	Volume (cm^3)	Target sonication (%)	
		Time-reversal	MMDM
Insula	0.875	34.33	51.4
Hippocampus	3.85	40.17	41.8
Caudate	4.73	3	25.4
Amygdala	0.491	51.48	65.3

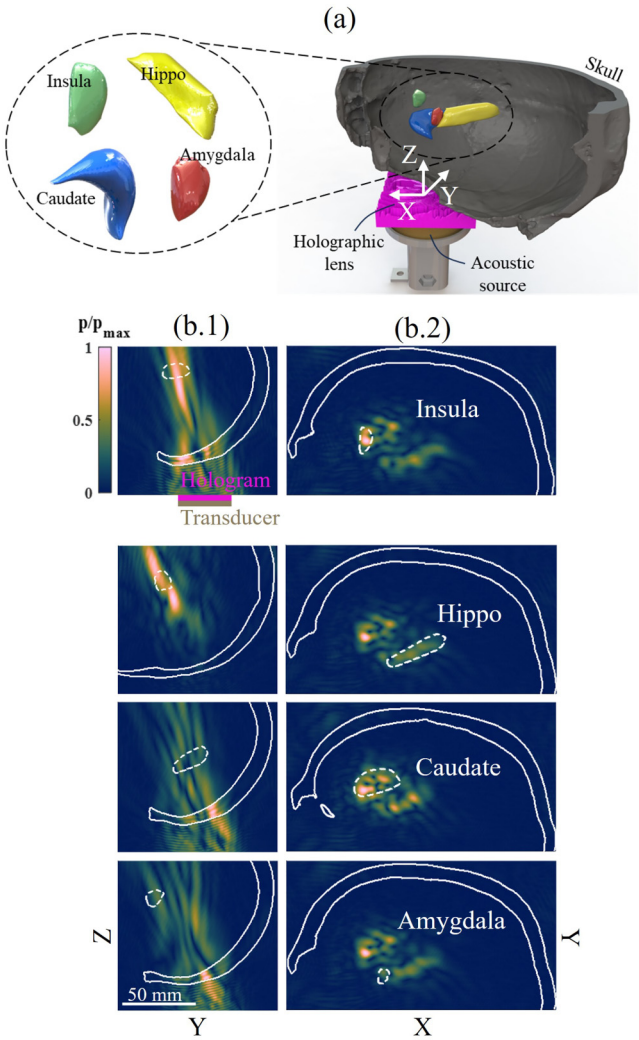

FIG. 4. Targeting results for four brain regions within the skull using a single hologram. (a) The position of each target (insula, hippocampus, caudate, and amygdala) is shown in different colors. (b.1) Axial view and (b.2) transversal view of numerical pressure field distribution for each target. The targets are ordered as insula, hippocampus, caudate, and amygdala, with center coordinates specified as follows: insula (X = 2.5 mm, Y = 58 mm, Z = 83 mm), hippocampus (X = 38.5 mm, Y = 66.5 mm, Z = 75 mm), caudate (X = 10.5 mm, Y = 47 mm, Z = 61.5 mm), amygdala (X = 15.5 mm, Y = 72 mm, Z = 74.5 mm).

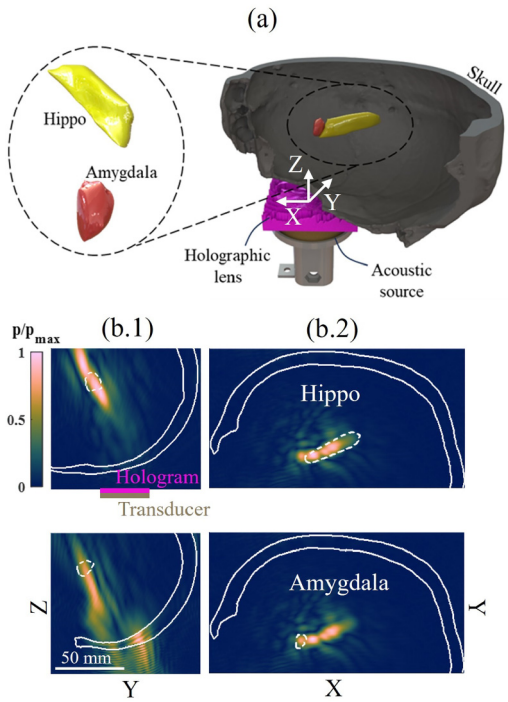

FIG. 5. Targeting results for two brain regions within the skull using a single hologram. (a) The position of two targets (hippocampus and amygdala) is shown in different colors. (b.1) Axial view and (b.2) transversal view of numerical pressure field distribution for each target. Center coordinates specified as follows: hippocampus (X = 38.5 mm, Y = 66.5 mm, Z = 75 mm) and amygdala (X = 15.5 mm, Y = 72 mm, Z = 74.5 mm).

However, when only two target volumes are considered good focusing of the acoustic energy is observed as shown in Fig. 5. The sonication of the total volume is also significantly improved to 42.26%. The results of the two case studies are summarized in Table IV.

H. Modified loss functions

A significant benefit of employing a gradient descent optimization scheme is the ability to tailor the optimization process by explicitly defining loss functions. This customization enables a biased targeting toward desired acoustic parameters. To demonstrate this advantage, we consider two cases in which the modification of the loss function improves a desired sonication parameter. Recalling the hippocampus results depicted in Fig. 2, significant energy leakage is observed outside the intended target. Better containment of the acoustic energy might be preferred for more precise procedures. To this end, the square loss function can be modified to

$$L(P3D,\, T) = \frac{1}{2}\sum_{i=1}^{n_X}\sum_{j=1}^{n_Y}\sum_{k=1}^{n_Z}\left(P3D_{ijk} - G_{ijk}T_{ijk}\right)^2, \tag{3}$$

where $G(X, Y, Z)$ is a 3D Gaussian distribution centered at the geometric centroid of the hippocampus. $G(X, Y, Z)$ is defined as

$$G(X,\, Y,\, Z) = \exp\left(-\left(\frac{(X-X_c)^2}{2\sigma_X^2} + \frac{(Y-Y_c)^2}{2\sigma_Y^2} + \frac{(Z-Z_c)^2}{2\sigma_Z^2}\right)\right), \tag{4}$$

where X_c, Y_c, Z_c are the coordinate of the geometric centroid, and σ_X, σ_Y, σ_Z are the standard deviations in X, Y, Z respectively. The standard deviation values were set to $\sigma_X = \sigma_Y = 2$ and $\sigma_Z = 20$. The Gaussian distribution acts as a weighing function that emphasizes the pressure at the centroid of the target and rapidly relaxes those requirements at further distances from the centroid. This approach prioritizes optimizing the containment of acoustic energy within the target, at the cost of the target's sonification volume. As shown in Fig. 6, by modifying the loss function the total sonicated volume outside the target decreased from 8.3 to 1.3 cm^3, while the sonication percentage degraded from 41.8% to 12.3%.

Similarly, the loss function can also be modified to prioritize the sonication of the target at the expense of energy leakage. To this end, a new modified loss function is implemented,

$$L(P3D,\, T) = \frac{1}{2}\sum_{i=1}^{n_X}\sum_{j=1}^{n_Y}\sum_{k=1}^{n_Z}\left(P3D_{ijk} - S_{ijk} + T_{ijk}\right)^2, \tag{5}$$

where S is defined as

$$S(X,\, Y,\, Z) = e^{-\frac{BW(X,Y,Z)^2}{2\sigma^2}}. \tag{6}$$

Here, we utilize a smoothing function S to modify the spatial extension of the binary target in the 3D volume. BW is the euclidean distance transform of the binary volume. For each voxel outside the target in the 3D spatial matrix, the distance transform assigns a value that corresponds to the distance between that voxel and the nearest nonzero voxel in the binary target. This formulation adds a smooth decaying extension at the boundaries of the binary target effectively creating a gradual transition zone. The decay rate is governed by the choice of the standard deviation σ which is set to 5.

TABLE IV. Summary of the numerical results for multi-focal targeting.

	Volume (cm^3)	Total sonicated volume (cm^3)	Sonication inside target (cm^3)	Percent of target sonication (%)	Gain inside target	Gain outside target
Four targets	9.95	6.42	0.78	7.82	2.58	3.08
Two targets	4.34	13.34	1.84	42.26	2.42	2.91

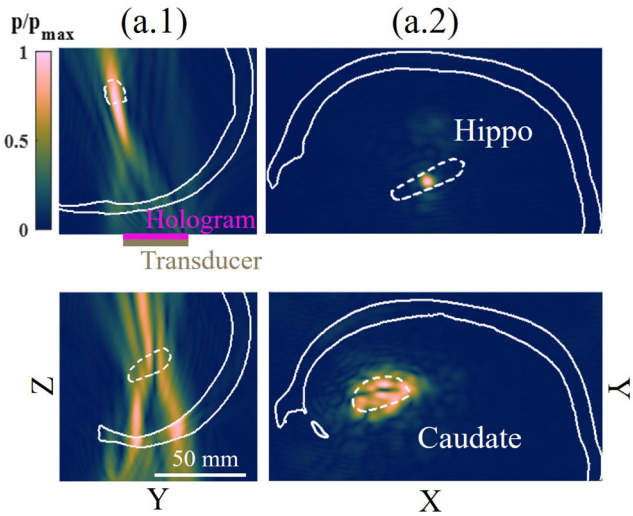

FIG. 6. Numerical results demonstrating targeting variation when modified loss functions are employed. The pressure field distribution for the hippocampus and caudate is shown in (a.1) for the axial view and (a.2) for the transversal view.

As shown in Fig. 6, when compared to the square loss function implementation, the modified optimization increases the Caudate sonification from 25.4% to 41.2%, however, the total sonicated volume outside the target also increased from 7.61 cm^3 to 18.2 cm^3.

In the presented case studies, the architecture of the new loss functions was subtly modified through the incorporation of custom weighting functions. Nevertheless, it is possible to construct and implement more sophisticated loss functions, provided that their gradients remain computable.

I. Discussion

The pressure fields created by acoustic holograms are inherently constrained by the diffraction limit and must adhere to the Helmholtz equation and the principle of energy conservation. This implies that sound fields that do not conform to these fundamental principles are not physically viable. As a result, there will inevitably be differences between the theoretically desired target field and the actual field that is physically realized due to these inherent limitations and principles governing acoustic propagation. The sound field can be significantly improved and optimized by carefully considering key parameters such as the numerical aperture, operating frequency, and the location and orientation of both the transducer and the hologram in relation to the size, position, orientation, and geometry of the target volume. This rigorous calibration guarantees that the acoustic field is fine-tuned to meet the appropriate targeting characteristics, maximizing the treatment process's efficacy, precision, and safety.

The numerical results clearly show that acoustic holograms are more effective at restricting the focal region within the transversal portion than in the axial section, especially for bigger targets such as the hippocampus and caudate. The wider the target's extent and cross-sectional area in the transversal plane, the weaker the field's focus is, resulting in a lower gain and a focused zone that is more elongated and distributed in the axial direction, causing greater sonication outside the target volume. This impact can be minimized by increasing the numerical aperture (transducer size) or adjusting the operating frequency, albeit both of these modifications have limitations. Another technique is to orient the transducer so that its axis is parallel to the target's longest dimension, resulting in an elongated focal area that is substantially contained inside the target volume. However, this strategy has limitations; for example, targeting the hippocampus will necessitate passing through the parietal bone, which is thicker and more curved, which could lead to new complications and issues such as skull heating and mode convergence.

These constraints are inherent in acoustic holographic lenses, not the optimization algorithm itself. However, the optimization methodology provided here, with its explicitly defined loss function, provides a method for somewhat overcoming these limits. Different loss and weighting functions can be used to direct the optimization algorithm to prioritize specific ultrasonic parameters. For example, to promote axial resolution by giving axial errors more weight than transversal errors. This approach could provide better axial confinement at the expense of transversal containment. Other parameters, such as pressure uniformity and coverage, can also be optimized to fit specific therapeutic demands and objectives, resulting in a more specialized optimization process that improves the efficacy of ultrasonic applications. The loss functions can be customized further by designating regions with low pressure and directing the algorithm to avoid sonication in these areas. This adjustment provides more precise control over pressure distribution, protecting vital or sensitive areas from unwanted ultrasonic wave exposure. Furthermore, the proposed algorithm effectively eliminates the uncertainties inherent in time-reversal techniques, where the impact of the number, distribution, and locations of virtual sources on focusing parameters is unclear. Determining the optimal distribution of virtual sources for specific desired focusing parameters can be challenging due to the non-iterative nature of these techniques and the computational limitations associated with them.[45]

IV. EXPERIMENTAL VERIFICATION

A. Experimental setup

The experimental setup is submerged in a water tank, as shown in Fig. 7. The walls of the tank are partially covered with Aptflex F28 acoustic absorbing sheets manufactured by Precision Acoustics, Ltd. The water tank is filled with degassed and de-ionized water in a temperature-controlled environment. A custom-made holder is fabricated to hold the skull, the ultrasound transducer, and the holographic lens. The position of the transducer can be moved manually relative to the skull in the X, Y, and Z directions. The transducer is custom-made and composed of a single circular piezoelectric disc with a diameter of 60 mm and an operating frequency of 444 kHz. The transducer is excited with a sinusoidal pulse signal (20 cycles) by a signal generator (Keysight 33500B) and an amplifier (Electronics and Innovation A075). The

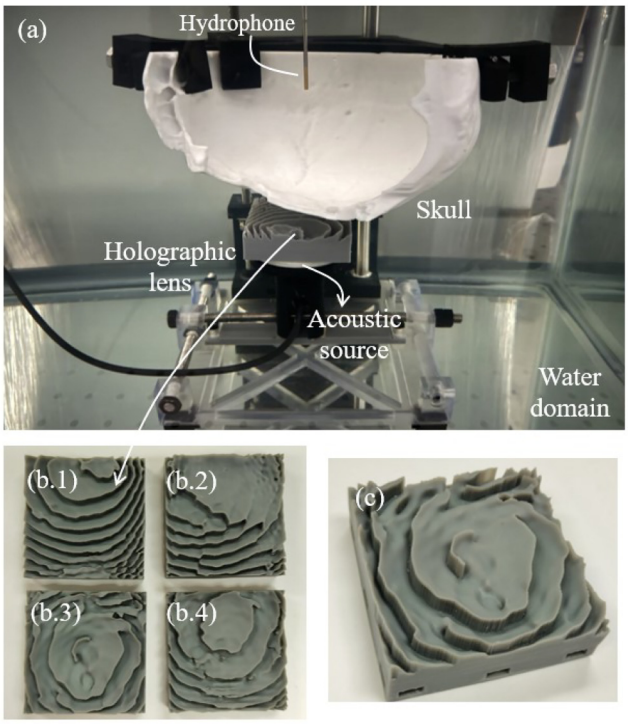

FIG. 7. (a) The experimental setup, including the acoustic source, 3D-printed acoustic hologram, 3D-printed skull phantom, and the hydrophone. The 3D-printed holograms for targeting the insula (b.1), hippocampus (b.2), caudate (b.3), and the amygdala (b.4). (c) Closeup of the 3D-printed hologram.

pressure field on a specified target plane is mapped with the ONDA HNR–0500 needle hydrophone attached to a custom-built in-house 3D positioning system. The measured signal from the hydrophone is sampled and digitized by a Tektronix TBS2104 oscilloscope and averaged 64 times to increase the signal-to-noise ratio. To eliminate the effect of any DC bias and higher frequency noises, the signal is post-processed using MATLAB by performing an FFT on the time series. A MATLAB program is used to control the positioning system and triggering of the function generator. The obtained voltage amplitude is then converted into acoustic pressure according to the calibration factor provided by the manufacturer (−250.13 dB). Various studies have utilized 3D printing capabilities to create skull phantoms, demonstrating the potential of 3D printing for replicating anatomical structures in experimental research.[46–48] In our work, the geometry of the skull is obtained using a segmented CT scan. A section of the skull is then 3D-printed with Polycarbonate (PC) FDM by STRATASYS (F270, Eden Prairie, MN) with a smooth hand finish. The acoustic properties of PC have been previously investigated underwater[49] with $c = 2380$ m/s, $\rho = 1153$ kg/m^3, and $\alpha = 12.23$ dB/cm at 1.1 MHz. A Formlabs (Formlabs, Somerville, MA, US) Form 3 gray resin was used for printing the acoustic lenses with a lateral and axial resolution of 25 microns. The acoustic properties of the resin were previously reported in an underwater experimental study[50] with $c = 2591$ m/s, $\rho = 1178$ kg/m^3, and $\alpha = 2.922$ dB/cm at 1 MHz.

B. Experimental results

Four holograms are designed based on the numerical results to validate the proposed algorithm. Underwater pressure scans in both the transversal and axial directions are carried out for each target using a hydrophone attached to a positioning system. Due to the hydrophone's limited mobility range within the skull, only smaller portions surrounding the target location are scanned. The experimental measurements are then compared to numerical simulations. Figures 8(a) and 8(b), respectively, show the geometry of the four target volumes and their corresponding location inside the 3D-printed skull phantom. Figures 8(c)–8(f), respectively, compare the experimental measurements and their corresponding numerical results for the insula, hippocampus, caudate, and amygdala. Good overall agreement is observed between the experimental measurements and the numerical results. The maximum experimental pressures measured in the transversal plane were 85.2 kPa for the insula, 98.5 kPa for the hippocampus, 127 kPa for the caudate, and 98.2 kPa for the amygdala with an excitation input of 200 V_{pp}. Scanning acoustic pressure underwater with a hydrophone and positioning system is a time-intensive process, permitting only one or a few 2D scan planes to be measured. Thus, for a quantitative comparison between experimental and numerical results, we calculated the focusing efficiency[24] in the transversal section. By comparing the acoustic power within the focal region to the total acoustic power in the entire plane. The calculations assume planar wave propagation. The focusing efficiency is given as

$$\eta = \frac{\Pi_{focal}}{\Pi_{total}} = \frac{\sum P^2_{focal}(X, Y, Z_0)}{\sum P^2(X, Y, Z_0)}. \tag{7}$$

The numerical and experimental focusing efficiencies of each target are summarized in Table V, where $P_{focal}(X, Y, Z_0)$ and Π_{focal} are the acoustic pressure distribution and the acoustic power in the focal regions, respectively. Π_{total} is the total acoustic power in the transversal plane. Examining Fig. 8(a), which presents insula results, we notice more pressure leakage outside of the focal region in the experimental data. This is evident from the disparity in focusing efficiency, with the simulations calculated at 76.5% compared to 46.1% in the experimental measurements. A similar pattern is observed in other test cases: the hippocampus has a numerical efficiency of 84.2% compared to an experimental efficiency of 49.2%, and the amygdala with a numerical efficiency of 70.1% against an experimental efficiency of 41.6%. Interestingly, the caudate is the only test case where the experimental results outperform the simulations, with an efficiency of 64.2% vs 57.1%, potentially due to a more pronounced top lobe in the experimental data as shown in Fig. 8(c). The differences between experimental and numerical results could be attributable to factors such as measurement mistakes, alignment challenges, variances in material qualities, and flaws in the produced skull phantom and hologram.

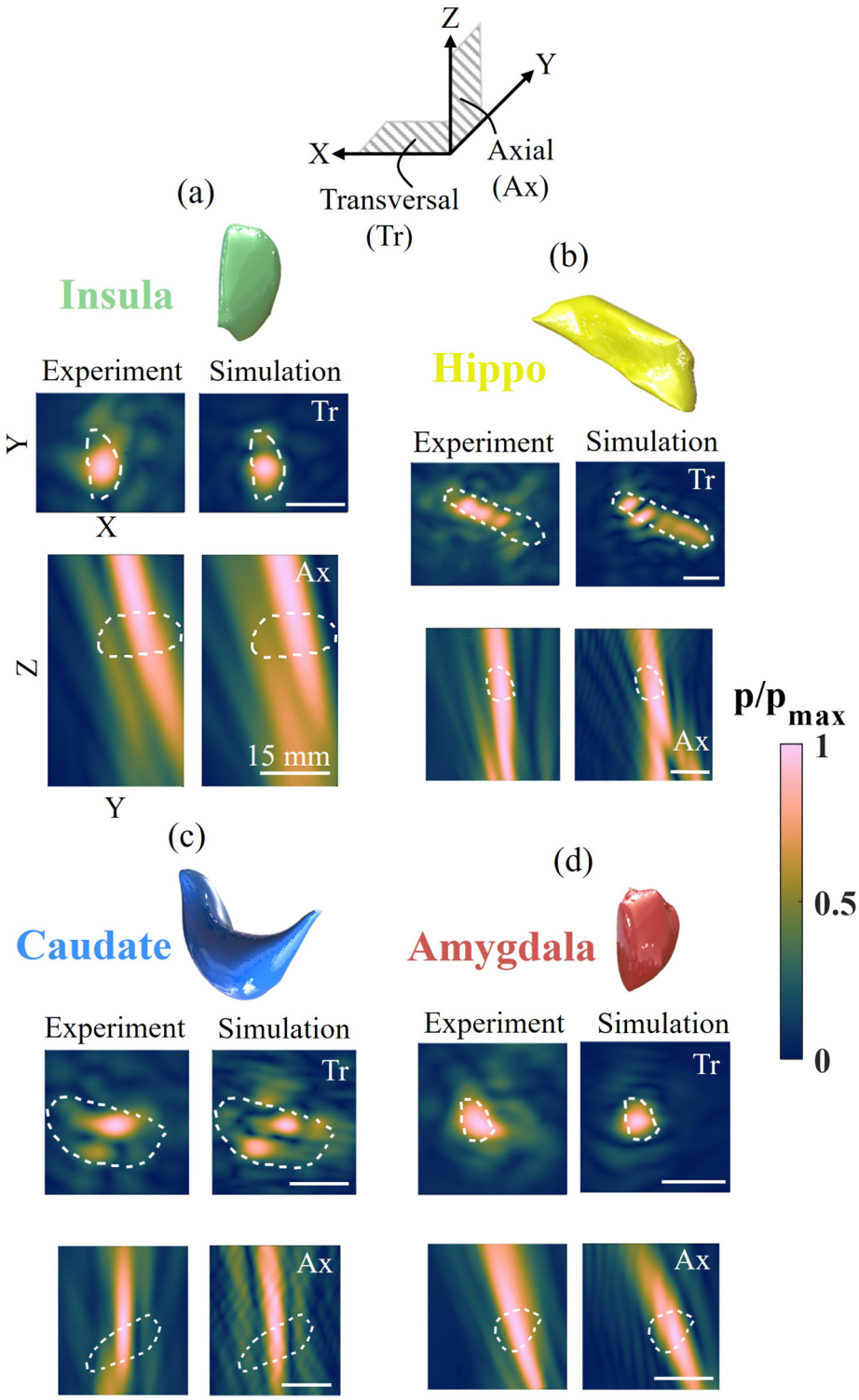

FIG. 8. Experimental and numerical results for the test cases of the (a) insula, (b) hippocampus, (c) caudate, and (d) amygdala.

TABLE V. Numerical vs experimental focusing efficiencies.

	Focusing efficiency (%)	
	Experimental	Numerical
Insula	46.1	76.5
Hippocampus	49.2	84.2
Caudate	64.2	57.1
Amygdala	41.6	70.1

V. CONCLUSIONS

We introduced an efficient volumetric holographic technique for creating 3D-printed acoustic holograms specifically for low-intensity non-thermal tFUS applications. The fundamental goal of these acoustic lenses is to generate precise FUS fields within the brain while successfully compensating for aberrations induced by the skull's structure. The proposed optimization strategy uses the modified mixed domain method to perform efficient ultrasonic propagation in strongly heterogeneous media, which is then incorporated into a gradient descent iterative volumetric holography optimization algorithm. The holographic approach outperforms the previously reported time-reversal strategies used in full-wave time-domain numerical simulations. Using the proposed approach, a hologram can be created in less than 50 min. Furthermore, due to the more efficient propagation, iterative optimization techniques can be used with explicitly assigned loss functions. The optimization technique can be fine-tuned to prioritize individual ultrasound characteristics by using different loss and weighting functions. For example, increasing axial resolution entails giving greater weight to axial errors than transversal ones, which improves axial containment but may reduce transversal containment. Other factors like pressure uniformity and coverage can also be adjusted to suit particular therapeutic requirements, enabling a more customized optimization process. The loss functions can also be specifically tailored to designate regions where minimal pressure is crucial, thereby directing the algorithm to prevent sonication in those sensitive areas, ensuring a more precise and effective ultrasound treatment. We applied the proposed algorithm to target four brain structures: the anterior insula, hippocampus, caudate nucleus, and amygdala. Verification was done through underwater experiments using a 3D-printed skull phantom that mimics the geometric features of a real skull. Good agreement was observed between the numerical results and the measured experimental data. Our results demonstrate that the acoustic holograms achieved effective coverage and confinement in the transversal plane. However, in the axial direction, sonication leakage varied depending on the target geometry, orientation, and volume, with lower axial containment observed in larger and transversely elongated targets like the hippocampus and caudate. It is crucial to recognize that the acoustic properties of the 3D-printed skull phantom differ from those of actual *in vivo* skulls. Differences in sound speed, density, and the presence of inhomogeneities and porosity in real skulls are significant factors. Future work will extend the present effort to include real skulls. The proposed approach enables more rapid computation of acoustic holograms, enabling quicker administration of therapeutic procedures and allowing for more flexibility in tailoring ultrasound fields for specific therapeutic requirements.

SUPPLEMENTARY MATERIAL

See the supplementary material for a more detailed analysis of pressure maps from time-reversal simulations and a comparison of numerical results with and without the skull for all four targets.

ACKNOWLEDGMENTS

This work was supported by the U.S. National Science Foundation (NSF) under CAREER grant Award No. CMMI 2143788, which is gratefully acknowledged.

AUTHOR DECLARATIONS

Conflict of Interest

The authors have no conflicts to disclose.

Author Contributions

Ahmed Sallam: Conceptualization (lead); Data curation (lead); Formal analysis (lead); Investigation (lead); Methodology (lead); Software (lead); Validation (lead); Visualization (lead); Writing – original draft (lead). **Ceren Cengiz:** Conceptualization (equal); Data curation (equal); Formal analysis (equal); Investigation (equal); Software (equal); Validation (equal); Writing – review & editing (equal). **Mihir Pewekar:** Conceptualization (equal); Data curation (equal); Investigation (equal); Software (equal); Validation (equal); Visualization (equal); Writing – review & editing (equal). **Eric Hoffmann:** Conceptualization (equal); Data curation (equal); Methodology (equal); Software (equal); Validation (equal). **Wynn Legon:** Conceptualization (equal); Funding acquisition (equal); Investigation (equal); Project administration (equal); Resources (equal); Supervision (equal); Writing – review & editing (equal). **Eli Vlaisavljevich:** Conceptualization (equal); Funding acquisition (equal); Investigation (equal); Project administration (equal); Resources (equal); Supervision (equal); Writing – review & editing (equal). **Shima Shahab:** Conceptualization (supporting); Funding acquisition (lead); Methodology (supporting); Project administration (lead); Resources (lead); Supervision (lead); Writing – review & editing (equal).

DATA AVAILABILITY

The data that support the findings of this study are available from the corresponding author upon reasonable request.

REFERENCES

[1]Y. Meng, K. Hynynen, and N. Lipsman, Nat. Rev. Neurol. **17**, 7 (2021).
[2]G. Darmani, T. Bergmann, K. B. Pauly, C. Caskey, L. De Lecea, A. Fomenko, E. Fouragnan, W. Legon, K. Murphy, T. Nandi *et al.*, Clin. Neurophysiol. **135**, 51 (2022).
[3]W. Legon, T. F. Sato, A. Opitz, J. Mueller, A. Barbour, A. Williams, and W. J. Tyler, Nat. Neurosci. **17**, 322 (2014).
[4]W. Lee, H.-C. Kim, Y. Jung, Y. A. Chung, I.-U. Song, J.-H. Lee, and S.-S. Yoo, Sci. Rep. **6**, 34026 (2016).

[5]J. Mueller, W. Legon, A. Opitz, T. F. Sato, and W. J. Tyler, Brain Stimul. **7**, 900 (2014).
[6]W. Legon, L. Ai, P. Bansal, and J. K. Mueller, Hum. Brain Mapp. **39**, 1995 (2018).
[7]T. Deffieux and E. E. Konofagou, IEEE Trans. Ultrason., Ferroelectr., Freq. Control **57**, 2637 (2010).
[8]W. Legon, S. Adams, P. Bansal, P. D. Patel, L. Hobbs, L. Ai, J. K. Mueller, G. Meekins, and B. T. Gillick, "A retrospective qualitative report of symptoms and safety from transcranial focused ultrasound for neuromodulation in humans," Sci. Reports **10**(1), 5573 (2020).
[9]W. Legon, P. Bansal, R. Tyshynsky, L. Ai, and J. K. Mueller, Sci. Rep. **8**, 10007 (2018).
[10]A. Strohman, B. Payne, A. In, K. Stebbins, and W. Legon, J. Neurosci. **44**, 8 (2024).
[11]N. Lipsman, M. L. Schwartz, Y. Huang, L. Lee, T. Sankar, M. Chapman, K. Hynynen, and A. M. Lozano, Lancet Neurol. **12**, 462 (2013).
[12]Z. Xu, T. L. Hall, E. Vlaisavljevich, and F. T. Lee Jr, Int. J. Hyperthermia **38**, 561 (2021).
[13]Y. Kim, T. L. Hall, Z. Xu, and C. A. Cain, IEEE Trans. Ultrason., Ferroelectr., Freq. Control **61**, 582 (2014).
[14]J. R. Sukovich, C. A. Cain, A. S. Pandey, N. Chaudhary, S. Camelo-Piragua, S. P. Allen, T. L. Hall, J. Snell, Z. Xu, J. M. Cannata *et al.*, J. Neurosurg. **131**, 1331 (2018).
[15]A. Kyriakou, E. Neufeld, B. Werner, M. M. Paulides, G. Szekely, and N. Kuster, Int. J. Hyperthermia **30**, 36 (2014).
[16]S. Almquist, D. L. Parker, and D. A. Christensen, J. Ther. Ultrasound **4**, 1 (2016).
[17]G. Maimbourg, A. Houdouin, T. Deffieux, M. Tanter, and J.-F. Aubry, Phys. Med. Biol. **63**, 025026 (2018).
[18]G. Kook, Y. Jo, C. Oh, X. Liang, J. Kim, S.-M. Lee, S. Kim, J.-W. Choi, and H. J. Lee, Microsyst. Nanoeng. **9**, 45 (2023).
[19]Z. Hu, Y. Yang, L. Xu, Y. Hao, and H. Chen, Front. Neurosci. **16**, 984953 (2022).
[20]S. Jiménez-Gambín, N. Jiménez, A. N. Pouliopoulos, J. M. Benlloch, E. E. Konofagou, and F. Camarena, IEEE Trans. Biomed. Eng. **69**, 1359 (2021).
[21]J. He, J. Wu, Y. Zhu, Y. Chen, M. Yuan, L. Zeng, and X. Ji, IEEE Trans. Ultrason., Ferroelectr., Freq. Control **69**, 662 (2021).
[22]S. Jiménez-Gambín, N. Jiménez, J. M. Benlloch, and F. Camarena, Phys. Rev. Appl. **12**, 014016 (2019).
[23]S. Jiménez-Gambín, N. Jiménez, and F. Camarena, Phys. Rev. Appl. **14**, 054070 (2020).
[24]A. Sallam, V. C. Meesala, M. R. Hajj, and S. Shahab, Appl. Phys. Lett. **119**, 144101 (2021).
[25]A. Sallam, V. C. Meesala, and S. Shahab, in *Active and Passive Smart Structures and Integrated Systems XV* (SPIE, 2021), Vol. 11588, pp. 1158807.
[26]A. Sallam and S. Shahab, Appl. Phys. Lett. **121**, 204101 (2022).
[27]K. Melde, A. G. Mark, T. Qiu, and P. Fischer, Nature **537**, 518 (2016).
[28]M. Bakhtiari-Nejad, A. Elnahhas, M. R. Hajj, and S. Shahab, J. Appl. Phys. **124**, 244901 (2018).
[29]K. Melde, H. Kremer, M. Shi, S. Seneca, C. Frey, I. Platzman, C. Degel, D. Schmitt, B. Schölkopf, and P. Fischer, Sci. Adv. **9**, eadf6182 (2023).
[30]J. Kim, S. Kasoji, P. G. Durham, and P. A. Dayton, Appl. Phys. Lett. **118**, 051902 (2021).
[31]D. Andrés, J. Vappou, N. Jiménez, and F. Camarena, Appl. Phys. Lett. **120**, 084102 (2022).
[32]C. Cengiz and S. Shahab, J. Phys. D: Appl. Phys. **57**, 365501 (2024).
[33]B. E. Treeby and B. T. Cox, J. Biomed. Opt. **15**, 021314 (2010).
[34]A. Sallam and S. Shahab, IEEE Trans. Ultrason., Ferroelectr., Freq. Control **70**(11), 1516–1526 (2023).
[35]J. Gu and Y. Jing, J. Acoust. Soc. Am. **147**, 4055 (2020).
[36]J. Gu and Y. Jing, IEEE Trans. Ultrason., Ferroelectr., Freq. Control **65**, 1258 (2018).
[37]J. Gu and Y. Jing, IEEE Trans. Ultrason., Ferroelectr., Freq. Control **68**, 1476 (2021).
[38]J.-F. Aubry, O. Bates, C. Boehm, K. Butts Pauly, D. Christensen, C. Cueto, P. Gélat, L. Guasch, J. Jaros, Y. Jing *et al.*, J. Acoust. Soc. Am. **152**, 1003 (2022).
[39]J. Zhang, N. Pégard, J. Zhong, H. Adesnik, and L. Waller, Optica **4**, 1306 (2017).
[40]A. D. Craig, Nat. Rev. Neurosci. **10**, 59 (2009).
[41]L. Q. Uddin, Nat. Rev. Neurosci. **16**, 55 (2015).
[42]H. Eichenbaum, T. Otto, and N. J. Cohen, Behav. Neural Biol. **57**, 2 (1992).
[43]J. A. Grahn, J. A. Parkinson, and A. M. Owen, Prog. Neurobiol. **86**, 141 (2008).
[44]P. H. Janak and K. M. Tye, Nature **517**, 284 (2015).
[45]D. Andrés, N. Jiménez, J. M. Benlloch, and F. Camarena, Ultrasound Med. Biol. **48**, 872 (2022).
[46]G. Mukwada, A. Hirst, P. Rowshanfarzad, and M. A. Ebert, Phys. Eng. Sci. Med. **47**, 455–463 (2024).
[47]J. Zhang, B. Yang, H. Li, F. Fu, X. Shi, X. Dong, and M. Dai, Sci. Rep. **7**, 4608 (2017).
[48]J. S. Naftulin, E. Y. Kimchi, and S. S. Cash, PLoS One **10**, e0136198 (2015).
[49]A. Antoniou, N. Evripidou, M. Giannakou, G. Constantinides, and C. Damianou, J. Acoust. Soc. Am. **149**, 2854 (2021).
[50]M. Bakaric, P. Miloro, A. Javaherian, B. T. Cox, B. E. Treeby, and M. D. Brown, J. Acoust. Soc. Am. **150**, 2798 (2021).
[51]See http://www.k-wave.org/ for the MATLAB toolbox k-Wave.